1 ***F*-region ionosphere effects on the mapping accuracy of SuperDARN HF radar echoes**

2

3 X.-C. Chen[1,2,3], D. A. Lorentzen[1,2,4], J. I. Moen[1,3], K. Oksavik[1,2], L. J. Baddeley[1,2,4] and M.

4 Lester[5]

5

6 1. Department of Arctic Geophysics, University Centre in Svalbard, Longyearbyen, Norway

7 2. Birkeland Centre for Space Science, Department of Physics and Technology, University

8   of Bergen, Bergen, Norway

9 3. Department of Physics, University of Oslo, Oslo, Norway

10 4. British Antarctic Survey, Cambridge, United Kingdom

11 5. Department of Physics and Astronomy, University of Leicester, Leicester, United

12   Kingdom

13

14 Corresponding Author: X.-C. Chen, Department of Arctic Geophysics, University Centre in

15 Svalbard, Longyearbyen, N-9171, Norway (xiangcai.chen@unis.no)

16

Abstract Structured particle precipitation in the cusp is an important source for the generation of F-region ionospheric irregularities. The equatorward boundaries of broad Doppler spectral width in Super Dual Auroral Radar Network (SuperDARN) data and the concurrent OI 630.0 nm auroral emission are good empirical proxies for the dayside open-closed field line boundary (OCB). However, SuperDARN currently employs a simple virtual model to determine the location of its echoes, instead of a direct calculation of the radio wave path. The varying ionospheric conditions could influence the final mapping accuracy of SuperDARN echoes. A statistical comparison of the offsets between the SuperDARN Finland radar spectral width boundary (SWB) and the OI 630.0 nm auroral emission boundary (AEB) from a meridian-scanning photometer (MSP) on Svalbard is performed in this paper. By restricting the location of the 630.0 nm data to be near local zenith where the MSP has the highest spatial resolution, the optical mapping errors were significantly reduced. The variation of the SWB – AEB offset confirms that there is a close relationship between the mapping accuracy of the HF radar echoes and solar activity. The asymmetric variation of the SWB – AEB offset versus magnetic local time suggests that the intake of high density solar extreme ultraviolet ionized plasma from post-noon at sub-auroral latitudes could result in a stronger refraction of the HF radar signals in the noon sector. While changing the HF radar operating frequency also has a refraction effect that contributes to the final location of the HF radar echoes.

1. Introduction

The Super Dual Auroral Radar Network (SuperDARN) has been a very successful tool for monitoring dynamical processes in the polar ionosphere [e.g., Greenwald et al., 1985, 1995; Chisham et al., 2007]. For SuperDARN, being an over-the-horizon radar system, the background ionospheric electron density is a crucial factor for the propagation of the HF radio waves [e.g., Milan et al., 1997; Danskin et al., 2002; Koustov et al., 2014]. By using transmitter frequencies between 8 and 20 MHz, SuperDARN is sensitive to field-aligned plasma density irregularities on the Bragg scale [Greenwald et al., 1985; Chisham et al., 2007]. The maximum backscatter power is returned when the refracted radio wave vector is nearly orthogonal to the local Earth's magnetic field [Greenwald et al., 1995]. The ionospheric backscatter therefore depends on both the occurrence of the field-aligned plasma density irregularities [e.g., Baker et al., 1986, Moen et al., 2002] and gradients in the ionospheric electron density [e.g., Ponomarenko et al., 2009].

SuperDARN typically uses a seven-pulse transmitter sequence to determine the complex autocorrelation function (ACF) of the echoes [Greenwald et al., 1985]. The derivative of the ACF phase with respect to time lag is used to estimate the Doppler line-of-sight velocity [e.g., Greenwald et al., 2008], while the decay time of the ACF power gives the Doppler spectral width [e.g., Baker et al., 1995; Ponomarenko and Waters, 2006]. For more than two decades, these data products have been widely used by the international scientific community. Applications, for instance, include the determination of global maps of ionospheric convection [e.g., Cousins and Shepherd, 2010] and studies of the variation of the polar cap area during substorm cycles [e.g., Milan et al., 2003b].

63 An area of significant emphasis in the literature is the equatorward boundary of OI 630.0 nm

64 cusp auroral forms, which is believed to be the ionospheric footprint of the open-closed field

65 line boundary (OCB) [Lorentzen et al., 1996; Milan et al., 1999; Moen et al., 1996, 1998 and

66 2001; Oksavik et al., 2000, 2004a]. On the poleward side of the ionospheric OCB the cusp

67 plasma becomes hot [Moen et al., 2004], which is indicative of enhanced magnetopause

68 reconnection [Lockwood et al., 1989]. In principle, this boundary should be easy to detect

69 also from SuperDARN data, and many investigations have looked at the co-location of the HF

70 radar cusp and the cusp aurora [e.g., Rodger et al., 1995; Milan et al., 1999; Moen et al., 2001,

71 2002; Oksavik et al., 2004b]. These studies have compared the location of the transition from

72 narrow to broad HF radar spectral width with the concurrent OI 630.0 nm auroral emission

73 boundary (AEB). Surprisingly often, there is an offset in latitude.

74

75 Rodger et al. [1995] observed HF radar echo boundaries that on average were 0.5°

76 equatorward of the optical AEB, which agrees with Oksavik et al. [2004b]. Conversely, Milan

77 et al. [1999] and Moen et al. [2001] found the optical AEB was located slightly equatorward

78 of the HF radar cusp. Moen et al. [2001] also tried to compensate by assuming different

79 auroral emission altitudes. Oksavik et al. [2011] used a ground range offset of 140 km to align

80 the HF radar echo with optical signatures associated with a reversed flow event. Statistically,

81 Chisham et al. [2005a, 2005c] and Sotirelis et al. [2005] confirmed that a close relationship

82 between the spectral width boundary (SWB) and the ionospheric open-closed field line

83 boundary (OCB) from the Defense Meteorological Satellite Program (DMSP) particle

84 precipitation data. Chisham et al. [2005a, 2005c] showed that the HF radar SWB was ~1°

85 latitude poleward of the DMSP particle precipitation boundary (PPB). Sotirelis et al. [2005]

86 observed that the offset varies from zero near noon to ~1° near dawn and dusk. Yeoman et al.

87 [2001] used the European Incoherent Scatter Heating facility to produce artificial

88   irregularities, and they found a ground range error of 114 km for 1½-hop SuperDARN echoes.

89   Consequently, the subsequent similar experiments imply that the SuperDARN ground range

90   error is often underestimated due to the varying ionospheric conditions [Yeoman et al., 2008].

91   However, the interrelationship of the varying ionospheric densities gives rise to the varied

92   mapping errors is still not well understood [Chisham et al., 2008].

93

94   It is well-known that the high-latitude F-region ionosphere is influenced by both

95   magnetospheric convection and particle precipitation [e.g., Lockwood et al., 1990; Cowley,

96   2000]. Two different categories of ionospheric plasma are thus comprised. Due to

97   magnetospheric convection a low density background plasma and a high density solar

98   extreme ultraviolet (EUV) ionized plasma that flows through the cusp inflow region and into

99   the polar cap from sub-auroral latitudes [Knudsen, 1974; Foster, 1984; Sojka et al., 1994].

100   During geomagnetic storms the high density plasma can form a continuous tongue-of-

101   ionization (TOI) that extends into the polar cap and greatly enhance the F-region electron

102   density [Foster et al., 2004, 2005]. The TOI can be further restructured into polar cap patches

103   when it crosses the dayside OCB [Carlson et al., 2004, 2006; Moen et al., 2006; Lorentzen et

104   al., 2010; Oksavik et al., 2006, 2010; Zhang et al., 2011, 2013a, 2015]. Nevertheless, soft

105   electron precipitation (having energy less than several hundred eV [Newell and Meng, 1992])

106   only adds structured plasma in the cusp ionosphere, compared to sub-auroral latitudes [Zhang

107   et al., 2013b]. They will produce 10-m scale plasma irregularities at km scale electron density

108   gradients in the F-region, which was recently verified by Moen et al. [2012] and Oksavik et al.

109   [2012] using high-resolution data from the ICI-2 sounding rocket.

110

111   The ground projection of SuperDARN echoes is currently determined by assuming a straight-

112   line propagation of the radio wave to a fixed virtual height (400 km at far ranges). It does not

113   account for the prevailing conditions in the ionosphere, which will give rise to varied mapping

114   errors compared to the actual location of the ionospheric plasma irregularities [e.g., Yeoman

115   et al., 2001, 2008; Chisham et al., 2008]. Ray tracing based on model electron densities could

116   in principle improve the ground projection of HF radar echoes [Villain et al., 1984; Liu et al.,

117   2012], but accurate determination of the propagation path within the highly varying

118   background ionosphere is difficult at far ranges [André et al., 1997; Ponomarenko et al.,

119   2009]. Furthermore, model like the International Reference Ionosphere (IRI) only describes

120   the ionospheric electron densities as monthly averages [Bilitza et al., 2014], which does not

121   account for the time-varying conditions in the ionosphere.

122

123   The SuperDARN Finland radar overlaps the field-of-view of a meridian scanning photometer

124   (MSP) in Svalbard, an alternative method for measuring the mapping accuracy of HF radar

125   echoes was recently introduced by Chen et al. [2015]. With high spatial resolution when the

126   aurora is near local zenith, the mapping error due to the assumed auroral emission height

127   becomes insignificant [Johnsen and Lorentzen, 2012a; Chen et al., 2015]. It allows for the

128   offset between the HF radar echoes and the auroral emissions to be quantified. By using

129   simultaneous observations of ground-based optical and HF radar OCBs along the

130   geomagnetic meridian, Chen et al. [2015] suggested that transient dayside reconnection could

131   segment the intake of solar EUV ionized plasma from sub-auroral latitudes, increasing the

132   background ionospheric density, and give rise to an excessive mapping error. The mapping

133   has particular importance for studies using HF radar data on small and meso-scale size.

134   Improved mapping is required for accurate tracking of polar cap patches [e.g., Lorentzen et al.,

135   2010; Oksavik et al., 2010; Zhang et al., 2013a; Nishimura et al., 2014] and for space weather

136   forecasting [Moen et al., 2013].

137

138   The current paper investigates the long-term variation of the latitude offsets between the HF

139   radar SWB and the OI 630.0 nm AEB in the high-latitude dayside ionosphere and its

140   relationship to the varying background ionospheric condition. This statistical study gives an

141   overview of the instrumentation and data processing in section 2. The relationship of the

142   latitude offsets between the HF radar SWB and the concurrent OI 630.0 nm AEB with the

143   solar activity, MLT and different HF radar operating frequencies is analyzed and discussed in

144   sections 3 and 4, respectively. Section 5 summarizes the importance of the varied F-region

145   plasma density contribution to the SWB – AEB offset.

146

147   **2. Instrumentation and Data Processing**

148   **2.1. Spectral Width Data from the SuperDARN Finland Radar**

149   The SuperDARN Finland radar is located at Hankasalmi (62.3° N, 26.6° E). It is part of

150   CUTLASS (Co-operative UK Twin Located Auroral Sounding System), and it has been in

151   operation since 1995. In its most common operating mode the radar has 16 beams. Each beam

152   is approximately 3.2° wide in azimuth and starting from 12° west of geographic north, while a

153   pulse length of 300 μs corresponds to a radar range gate length of 45 km [Milan et al., 1997].

154   The first gate is located at 180 km range, and for each beam a total of 75 range gates is

155   usually recorded. The radar thus completes a full scan in either 60 or 120 s [Lester et al.,

156   2004]. This work only utilizes common mode data, which has been preprocessed using the

157   same version of the SuperDARN software (fitACF v.1.09, e.g., using the modifications to the

158   ACF processing as described by Ponomarenko and Waters [2006]). Beam 9 intersects the

159   Longyearbyen (LYR) MSP at the ~1890 km range (see Figure 1). From the received signal-

160   to-noise ratios the ionospheric plasma Doppler line-of-sight velocity, the Doppler spectral

161   power, and the Doppler spectral width can be derived [Greenwald et al., 1995].

162

2.2. Auroral Data from the Meridian Scanning Photometer (MSP)

The MSP is located at LYR (78.2º N, 15.8º E) and provides the ground-based optical observation of auroral boundaries. The MSP has a rotating mirror that scans along the geomagnetic meridian. The time resolution is 16 s, and the emission intensity is measured in Rayleigh for scan angles ranging from 0º to 180º (from north to south) at an angular resolution of ~1º. The background emissions were subtracted from the peak emissions using tilting interference filters [Romick, 1976]. Five channels, which include red (OI 630.0 nm) and green (OI 557.7 nm) auroral emissions, are recorded simultaneously. In 2007 the old Aurora Station was relocated to the new Kjell Henriksen Observatory (KHO, AACGM: 75.2º N, 111.1º E). Except for the 2005/2006 and 2006/2007 winter seasons, these optical data are available from 15 auroral seasons since 1994/1995.

2.3. Boundary Identifications

The equatorward boundaries of the OI 630.0 nm auroral emission and the latitude transition from narrow to broad spectral width must be simultaneously identified. For each MSP meridian scan, a search is performed to identify where the gradient of the emission intensity maximizes in order to trace the OI 630.0 nm AEB. The mapping height as a function of MSP scan angle, with a set of equations describing the mapping error, is used in this study (see Johnsen et al. [2012] for more details). The validity of this method has been confirmed by a number of case studies [Johnsen and Lorentzen, 2012a] and by statistical comparison [Johnsen and Lorentzen, 2012b]. To avoid the large mapping errors associated with MSP scan angles close to the horizon, only the boundaries from MSP scan angles between 40° and 150° were used (i.e. corresponding to the region directly overhead of the observation site, magnetic zenith at 98°). By means of trigonometry, the geographic latitude and longitude are calculated based on the assumed height for the emission (i.e. 303, 268, and 264 km at scan angles 40°,

188   zenith, and 150°, respectively). The Altitude Adjusted Corrected Geomagnetic (AACGM)

189   [Baker and Wing, 1989] latitude is used to project the OI 630.0 nm AEB and HF radar SWB

190   into the same coordinate system.

191

192   An improved method for automatically identifying the HF radar SWB along the MSP

193   meridian has been presented by Chen et al., [2015]. This method is similar to the Chisham and

194   Freeman [2003] 'C-F threshold technique', i.e. using a spectral width threshold value that

195   normally originates from typical cusp backscatter, and searching poleward along the radar

196   range gate until this threshold is exceeded. However, more criteria (see Chen et al., [2015] for

197   more details) are implemented to eliminate any false boundary identifications due to lack of

198   echoes, hence the problem with unreliable boundaries for beams away from the meridional

199   direction [Chisham et al., 2005b] can be avoided. A high time resolution (2 min) estimate of

200   the HF radar SWB is finally obtained [Chen et al., 2015].

201

202   In spite of the fact that the interpretation of the broad spectral width remains elusive, the

203   spectral width typically shows broad values around the cusp [e.g., Baker et al., 1995]. The

204   SWB represents a transition from low to high spectral width values with increased

205   geomagnetic latitude (MLAT) [e.g., Moen et al., 2001; Chisham and Freeman, 2004; Freeman

206   and Chisham, 2004]. Due to the fact that ionospheric irregularity lifetime is essentially

207   independent of the scale size [e.g., Vallières et al., 2003; Ponomarenko et al., 2007], the broad

208   spectral width values will decrease with increasing HF radar operating frequency.

209   Ponomarenko et al. [2007] found that the "normalized" spectral width, $F = 1/\tau_{corr} \approx 2\pi \cdot f_0 \cdot W/c$,

210   is more suitable for representing the spectral width W, which is determined by the irregularity

211   lifetime (τ_{corr}) mechanisms [Ponomarenko and Waters, 2006]. The f_0 is the radar frequency

212   and c is the speed of light, and taking 40 Hz as the typical "normalized" spectral width

213   [Ponomarenko et al., 2007], the selected spectral width threshold values linearly varied

214   between 150 and 200 m/s with the HF radar operating frequency in the current study.

215

216   The time interval chosen for this study was 12:00 ± 3 MLT (magnetic noon at LYR is ~09:00

217   UT). By manual removal of days with bad, missing or otherwise unusable optical data, and

218   days without ionospheric backscatter, a total of 92 events (of different duration) of

219   simultaneous good optical and HF radar observations was chosen for the statistical analysis.

220   The optical and radar data were reduced to 2-min time resolution in order to ease the

221   comparison. Figure 2 shows an example of the simultaneous boundary determinations of AEB

222   and SWB (black dashed curves) from the two instruments.

223

224   **3. Results**

225   **3.1. Yearly Variability**

226   The number of usable days for each winter season is shown by bar plots in Figure 3a. Each

227   vertical red stem represents the corresponding number of comparable data points, with 2 min

228   time resolution between HF radar SWB and OI 630.0 nm AEB. The horizontal time axis

229   represents the winter auroral seasons from December to January. Due to instrument

230   malfunction, the data for winter seasons 05/06 and 06/07 are unavailable (see section 2.2).

231   The missing data for the 10/11 season is due to bad weather and few HF radar echoes.

232

233   The normalized yearly occurrences of the OI 630.0 nm AEB and HF radar SWB with 0.5°

234   latitude resolution are shown in Figures 3b and 3c, respectively. Figure 3b indicates that the

235   OI 630.0 nm AEB is located slightly north of geomagnetic zenith (AEB: 75.62° MLAT on

236   average), which is consistent with previous cusp particle precipitation data from the DMSP

237   satellites [e.g., Newell and Meng, 1992]. The envelope of the OI 630.0 nm AEB distribution

238 shifts to lower latitude for winter seasons 02/03, 11/12 and 13/14, which is approximately

239 associated with the enhanced $F_{10.7}$ solar radio flux seen in Figure 3e. This implies that the

240 solar wind driving during these years was significantly higher than the remaining interval,

241 thus expanding the polar cap due to the increased energy input [Milan et al., 2012]. The HF

242 radar SWB in Figure 3c displays a latitude distribution with the majority of SWBs around

243 77.29° MLAT, which is ~1.5° (i.e. ~160 km), on average, further poleward than the AEB.

244

245 The yearly variation of the median filtered SWB – AEB offset, with error bars representing

246 the standard deviation, is shown in Figure 3d. While Figure 3f shows the distribution of

247 comparable data points for different radar operating frequencies. Four frequencies (around

248 10.0, 11.2, 12.4 and 13.2 MHz) were mainly used during the winter season. When the $F_{10.7}$

249 solar flux increases, it can be seen that the SWB – AEB offset also shows a slight increase

250 (with the one exception being the winter season 98/99). To investigate the dependence on

251 solar cycle the winter seasons 99/00 – 03/04 (cycle 23) and 11/12 – 13/14 (cycle 24) will be

252 used as a proxy for Solar maxima [e.g., Bjoland et al., 2015], while the rest of the season for

253 Solar minima (i.e. 95/96 – 98/99 and 04/05 – 09/10). Using this definition, the averaged SWB

254 for solar maxima (minima) is found to be ~2° (~1°), on average, poleward of the AEB.

255

256 **3.2. Diurnal Variability**

257 The number of data points as a function of MLT, with the same colors as Figure 3f

258 representing different HF radar operating frequencies, is shown in Figures 4a and 4b for solar

259 maxima and minima, respectively. Only three frequencies were used at solar minima. The

260 distributions illustrate that most HF radar echoes occurred at ~11:00 – 14:00 MLT. An

261 asymmetric distribution of the data points at 12.4 (10.0) MHz radar frequency, indicates that

262 the occurrence of the HF radar echoes tends to be in the pre-noon (post-noon) sector for solar

263 maxima (minima).

264

265 To ensure reliable results, only intervals having more than 150 data points (red bars >150 in

266 Figure 4a, and black bars >150 in Figure 4b) were used for more specific comparison. The red

267 line in Figure 4c shows the mean AEB latitudes versus MLT for solar maxima and 12.4 MHz

268 radar frequency. The AEB is on average situated at ~75.48° MLAT, and slightly lower in the

269 pre-noon sector (~09:00 – 11:00 MLT) than in the noon and post-noon sectors (~11:00 –

270 15:00 MLT). The distribution of mean SWB (grey line) also shows a similar trend, which is

271 consistent with observations of Ruohoniemi and Greenwald [1997] (see their plate 5 in winter)

272 and Lointier et al. [2008] (see their Figure 1). The SWB – AEB offset in Figure 4e is smaller

273 in the pre-noon sector (~1.46° on average) than in the noon and post-noon sectors (~2.37°,

274 peak at 13:15 MLT).

275

276 For solar minima in Figure 4d the distributions satisfying the selecting criteria are

277 concentrated near noon, i.e. ~11:00 – 14:00 MLT. The mean AEB latitudes are located at

278 ~76.91°, 76.35° and 77.21° MLAT, respectively, for radar frequencies of 10.0 (black), 11.2

279 (green) and 12.4 (red) MHz. The concurrent SWB latitudes are not shown here to ensure

280 clarity in the Figure, but Figure 4f indicates that the mean SWB latitudes are located 0.62°

281 (peak at 12:55 MLT), 0.67° (peak at 12:55 MLT) and 1.47° (peak at 12:25 MLT) poleward of

282 the AEBs, respectively. Furthermore, the results in Figure 4e and 4f also show that the mean

283 SWB – AEB offset in the post-noon sector (12:00 – 15:00 MLT) is generally larger than in

284 the pre-noon sector (09:00 – 12:00 MLT).

285

286 **3.3. Range Variability**

287   Although the peak SWB – AEB offset does not correspond to the highest AEB latitude, the

288   increased SWB – AEB offset seems to be partly related to the poleward movement of the

289   boundary, which has previously been observed by Chisham et al. [2008] and Liu et al. [2012].

290   They attributed this difference to the standard virtual height model used in the radar

291   processing. In order to quantify the influence of the enhanced ionospheric density on the SWB

292   – AEB offset, Figure 5 shows scatter plots of the mean SWB – AEB offset versus AEB

293   latitude at solar maxima with radar frequency 12.4 MHz (red) and solar minima with radar

294   frequency 10.0 MHz (black). The dots show observations before 11:00 MLT, while the stars

295   show observation after that.

296

297   Looking at solar maxima it can be seen that the observations before and after 11:00 MLT

298   behave differently. Before 11:00 MLT there is only a small change in the auroral emission

299   boundary with respect to changes in the SWB – AEB offset. After 11:00 MLT there is a large

300   change in both the auroral emission boundary and the SWB – AEB offset with a slope

301   coefficient for the fit equal to 0.72 ± 0.31. The increased SWB – AEB offset near noon is

302   strongly related to the increasing ground range. However, for solar minima this trend is

303   reduced to a slope coefficient of 0.48 ± 0.36. Considering the relationship between a ray path

304   and the ground range [e.g., Chisham et al., 2008], the high coefficient is thought to be related

305   to a large elevation angle of the ray path. As the ionospheric electron density is typically

306   higher at solar maxima than minima [e.g., Cai et al., 2008], the increased SWB – AEB offset

307   strongly relies on the increasing ground range at solar maxima, which implies that the

308   enhanced ionospheric density modulates the HF radar ray path more strongly.

309

310   **3.4. Frequency Variability**

311   However, the comparison of SWB - AEB offsets at solar maxima and minima in Figure 5 are

312   for different radar frequencies. In order to investigate whether the varied radar frequencies

313   have potential impact on the final mapping accuracy of the SWBs, Figure 6 compares the

314   variation of median filtered SWB – AEB offsets with ranges (i.e. different AEB latitudes) at

315   the different radar operating frequencies. To reduce the probable influences of the changed

316   solar flux and MLT, the contrast has been confined to similar solar $F_{10.7}$ flux (i.e. 02/03 and

317   13/14 data used in the top panel, 01/02 used in the middle panel, 98/99 and 04/05 used in the

318   bottom panel) and the same MLT (i.e. 12:00 – 13:00 MLT). The line plot with error bars

319   represents the variation of the median filtered SWB – AEB offset with the AEB latitudes,

320   while the different colors represent the corresponding radar frequencies. The bar plot shows

321   the distribution of data points within each latitude.

322

323   It can be easily seen that there is no distinct linear trend for the SWB – AEB offset along with

324   the increased range. However, for nearly equal solar fluxes, i.e. for each panel, the SWB –

325   AEB offsets with high radar frequencies are larger than for low radar frequencies at the same

326   range, which means that the high radar frequency to a certain degree contributes to the final

327   range accuracy.

328

329   **3.5. A Case Study**

330   The SWB – AEB offsets versus MLT peak near noon (see Figures 4e and f). Figure 7 presents

331   an example of the SWB – AEB offset derived from Figure 2 and the simultaneous ionospheric

332   total electron content (TEC) observations from a GPS receiver at a lower latitude (Tromsø) to

333   illustrate the importance of the enhanced solar EUV high density plasma in the post-noon

334   sector (i.e. after ~09:00 UT). The IMF B_y and B_z component data from ACE, which was

335   situated at (238, -25.5, 20.6) R_E in GSM coordinates, are shown in Figure 7a. With a solar

336 wind speed of ~413 km/s, a ~61 min time lag from the satellite to the cusp ionosphere is

337 estimated using the equation given by Liou et al. [1998] and Lockwood et al. [1989]. The

338 southward IMF, with poleward moving auroral forms (see Figure 2a), is favorable for dayside

339 low-latitude reconnection [Sandholt et al., 1998]. IMF B_y is initially negative, but abruptly

340 changes to positive at 09:32 UT (~12:32 MLT), coincident with a sharp fall in IMF B_z to -6

341 nT.

342

343 The IMF clock angle, defined as $\theta = \tan^{-1}(|B_y/B_z|)$ for $B_z > 0$ and $\theta = 180º - \tan^{-1}(|B_y/B_z|)$ for

344 $B_z < 0$ in the GSM y-z plane, is given by the magenta curve in Figure 7b. It varies between

345 100° and 180°. The SWB – AEB offset, with error bars representing the potential mapping

346 errors from the assumed auroral altitude model, is overlaid in Figure 7b (black curve). The

347 fluctuations are stronger in the post-noon sector, where the averaged SWB – AEB offset

348 (~1.49°) increases twofold compared to the pre-noon sector (~0.67°). The simultaneously

349 estimated TEC values from the GPS receiver at the Tromsø site (see Figure 1, Glat.: 69.6°,

350 Glon.: 19.2°, Finland radar beam 5 intersects it at range ~945 km), provides an estimate of

351 TEC in 1 by 1 degree bins every 5 min [Rideout and Coster, 2006].

352

353 Figure 7c shows that the vertical ionospheric electron density increased from 3.75 TEC units

354 in the pre-noon sector to 6.74 TEC units in the post-noon sector. With the intake of high

355 density solar EUV ionized plasma from post-noon at sub-auroral latitudes [Foster, 1984;

356 Moen et al., 2006; Lorentzen et al., 2010; Oksavik et al., 2010; Zhang et al., 2011, 2013b;

357 Chen et al., 2015], some peaks of the SWB – AEB offset partly associated with the enhanced

358 IMF southward component are observed. This is particularly evident at 08:18, 09:04, 09:10,

359 09:36, and 09:46 UT where there is a clear correlation between the increased SWB – AEB

360 offset and the enhanced TEC.

4. Discussion

Based on the simultaneous ground observations of OI 630.0 nm AEB and HF radar SWB along the geomagnetic meridian, covering winter season data from 95/96 to 13/14, a time dependent statistical study of the SWB − AEB offset is performed. The ionospheric electron density as a crucial factor for SuperDARN HF radio wave propagation [e.g. Milan et al., 1997; Danskin et al., 2002; Koustov et al., 2014], the varied SWB − AEB offset should reflect the changed *F*-region ionospheric electron density due to solar activity and ionospheric convection.

4.1. Validity of Results

The careful reader will notice that our SWB − AEB offset has some discrepancies compared to prior statistical results [e.g., Chisham et al., 2005; Sotirelis et al., 2005; Yeoman et al., 2008]. The SWBs measured by Chisham et al. [2005c] and the CRBs derived by Sotirelis et al. [2005] were located 0 − 1° equatorward of the DMSP PPBs location near magnetic noon, which is smaller than the results presented here. However, by comparing with Yeoman et al. [2008]'s experiments that presented results from the same path (i.e. plasma irregularities generated by the SPEAR Heating facility in Longyearbyen on 17 April 2004), a difference in range accuracy (270 km in their Figs. 4aiv) that is larger than our median filtered SWB − AEB offset (1.57°, i.e. 170 km) in Figure 3 (03/04 winter season). These discrepancies could be due to different boundary finding algorithms and the database used. In our study, the acquired AEB is derived from a pre-defined reference model (see Johnsen et al. [2012] for more details), and an intimate relationship of the AEB with the PPB derived from the DMSP has been statistically confirmed by Johnsen and Lorentzen [2012] (see their Figure 7b). For SuperDARN data, the robust boundaries from both Chisham et al. [2005c] and Sotirelis et al.

386 [2005] were built at the cost of the temporal resolution of the boundary motion (10 min time

387 resolution, i.e. a median filter of adjacent beams and across 5 consecutive scans), while the

388 range accuracy from Yeoman et al. [2008] was employed by the high backscatter power for

389 each range gate. In our paper, the boundary finding algorithm adopts median filter to the

390 adjacent range gate along geomagnetic meridian with 2 min time resolution (see Chen et al.

391 [2015] for more details). On average the range accuracy should thus be larger than the results

392 of Chisham et al. [2005c] and Sotirelis et al. [2005], but smaller than Yeoman et al. [2008]. In

393 addition, we only used winter season data, the seasonal difference may also be one of the

394 potential factors affecting the ionospheric plasma density and the range accuracy.

395

396 The improved SuperDARN virtual height model for mapping accuracy of ionospheric

397 backscatter has also been derived and assessed by Chisham et al. [2008] and Yeoman et al.

398 [2008], respectively. However, the standard virtual height model is still used in our study

399 because the typical heights of natural and heater-induced ionospheric irregularities, as well as

400 the path geometry for SuperDARN radars, are different. Although the AEB elevation angles

401 have been confined, the assumed AEB height will inevitably introduce a mapping error at a

402 certain degree. If the final mapping error of the ionospheric backscatter measured by the

403 improved virtual height model is analogous to the AEB introduced error, the reason for the

404 SWB – AEB offset will be difficult to judge. Alternatively, a range correction algorithm using

405 elevation angles has also been provided by Yeoman et al. [2008]. However, not all elevation

406 angle data from Finland radar are calibrated and can be used in this study.

407

408 **4.2. Variation with Solar Cycle**

409 The results presented here indicate quantitively that the standard mapping technique utilized

410 by the SuperDARN HF radars (i.e. that the HF radar path propagates to a fixed height along a

411   straight line) produces some overestimation of the distances at far range [e.g., Chisham et al.,

412   2008; Yeoman et al., 2008; Liu et al., 2012]. Figure 3d shows that the SWB – AEB offset at

413   solar maxima is approximately two times larger than at solar minima (~2° vs. ~1°), even

414   though the target irregularities (i.e. AEB) are typically located at a lower latitude (see Figure

415   3b). This indicates that the real ray path is strongly refracted at solar maxima. The $F_{10.7}$ index

416   characterizes the solar EUV irradiance [Tobiska et al, 2000], which induces the vast majority

417   of ionization in the sunlit ionosphere. The yearly variations of SWB – AEB offsets and solar

418   flux, shown in Figures 3d and 3e with a Pearson correlation coefficient of 0.61, imply that the

419   real radio wave propagation path is modulated by the varying background ionospheric

420   conditions (see also Figure 7).

421

422   The dayside auroral zone is a hard target for coherent HF radars, and the propagation mode

423   could be changed between 1½-hop and ½-hop randomly [Milan et al., 1998]. However, the

424   SuperDARN Finland radar is inclined to 1½-hop propagation in the cusp region [e.g.,

425   Yeoman et al., 2001, 2008; Danskin et al., 2002]. Although the current dataset did not

426   consider possible changes in the propagation mode, the statistical result of Chisham et al.

427   [2008] showed that the mapping error from the SuperDARN standard virtual height model

428   (see their Figure 5 bottom panel), at ~1750 – 2200 km range (i.e. the majority of SWB

429   latitudes at ~74° – 78° MLAT) was almost equal to the 1½-hop and ½-hop propagation modes.

430   This means that the variable ionospheric density with solar activity is still a crucial reason for

431   the mapping errors.

432

433   The electron density and peak height in the high latitude F-region is typically higher at solar

434   maxima than minima [e.g., Cai et al., 2008], to achieve that the maximum HF radio wave

435   returns, the ionospheric refraction index must be stronger at solar maxima than minima

436   [Gillies et al., 2010], giving an increase in the returned ionospheric backscatter at higher

437   elevation angles [Ponomarenko et al., 2011]. This is also reflected in the observations that the

438   rate of increase of SWB – AEB offset versus AEB latitude is higher at solar maxima than

439   minima (see Figure 5 coefficients, 11:00 – 14:00 MLT). Statistical studies of the backscatter

440   height and elevation angle at solar minima by Liu et al. [2012] (height: ~239 km, angle: 8° –

441   10° on average) and at solar maxima (but only at midnight) by Koustov et al. [2007] (height:

442   ~275 km, angle: ~12° on average) illustrates that the enhanced solar activity influences the

443   peak F-region electron density. This in turn will influence the HF radio wave path and the

444   location at which it achieves near orthogonality with the local geomagnetic field. This

445   suggests that the mapping errors of the SWBs caused by the standard SuperDARN virtual

446   height model [Chisham et al., 2008; Liu et al., 2012], which is modulated by the varied

447   ionospheric condition due to the solar irradiance flux [Yeoman et al., 2008; Chen et al., 2015].

448

449   **4.3. Variation with MLT**

450   The distributions of data points in Figures 4a and 4b show that the cusp is the most likely

451   location for ionospheric HF radar echoes. The SWB – AEB offset becomes larger in the noon

452   and post-noon sectors than the pre-noon sector, while the peak SWB – AEB offsets (see

453   Figures 4e and 4f) are all near noon. Due to the dayside reconnection electric field that

454   controls the transport of EUV ionized plasma inflow from sub-auroral latitudes to cusp [e.g.,

455   Foster, 1984, 1993; Foster et al., 2005; Moen et al., 2006, 2008; Oksavik et al., 2010; Carlson

456   et al., 2006; Zhang et al., 2013, and references therein], the results imply that the low density

457   background plasma and high density solar EUV ionized plasma could be redistributed at noon

458   and post-noon sectors by ionospheric convection [Lockwood and Carlson, 1992, Pinnock et

459   al., 1995; Moen et al., 2008], which would make the HF radar ray intersect more enhanced

460   plasma in the cusp region.

461

462 A schematic explanation of the different *F*-region density structures is shown in Figure 8. The

463 color coded grids represent yearly averaged distributions of *F*-region ionospheric peak

464 electron density (NmF_2) from the IRI-2012 model. The general dawn-dusk (white-black)

465 convection cell derived from the SuperDARN convection model is overlaid. The fan-shaped

466 grey line represents the field-of-view of the SuperDARN Finland radar at 09:00 UT, while the

467 magenta arrows represent ionospheric convection through the cusp inflow region.

468

469 It can be easily seen that the high density solar EUV ionized plasma is a persistent feature at

470 sub-auroral latitude in the post-noon sector, while the dawn-side ionospheric convection is

471 mainly occupied by low density plasma. The distribution of NmF_2 is consistent with the

472 relatively large SWB – AEB offsets found in the noon and post-noon sectors, instead of the

473 pre-noon sector. However, the transport of high density solar EUV ionized plasma through the

474 cusp inflow region cannot distinctly reveal itself in IRI data, which has also been previously

475 analyzed by Moen et al. [2008] that the chance of magnetopause reconnection and new intake

476 of high density solar EUV ionized plasma decreases for IMF B_z positive. This could explain

477 why the observed linear variation of SWB – AEB offset with latitudes in Figure 5 is difficult

478 to see in Figures 6 and 7. The linear fit in Figure 5 illustrates the role of the enhanced

479 ionospheric density for HF radar ray path. As the solar EUV irradiance increases by as much

480 as a factor of 3 over a solar cycle [e.g., Woods et al., 2005], it can be seen that the mean SWB

481 – AEB offset at solar maxima is larger than at solar minima, even in the pre-noon sector,

482 which indicates that the increased SWB – AEB offset responds strongly to the enhanced

483 ionospheric density.

484

485   However, the AEB is notably suppressed to low latitude in the pre-noon hours (see Figure 4c).

486   This is a little lower than the statistical AEB results at the same MLT by Johnsen and

487   Lorentzen [2012b]. The reason is that not all observed auroral events can return the HF radar

488   echoes because of the relatively low density and varied background ionospheric conditions.

489   On the contrary, the decreased SWB – AEB offset in the post-noon sector (i.e. 14:00 – 15:00

490   MLT in Figure 4e) corresponds to the relatively stable AEB at high latitudes. The geophysical

491   factors that influence the discrepant variation of ionospheric density versus MLT should be

492   taken into account [e.g., Ruohoniemi and Greenwald, 1997; Koustov et al., 2014].

493

494   For the SuperDARN Finland radar the radio wave path is generally from low to high

495   geomagnetic latitude, whilst the horizontal F-region ionospheric density on the dayside is

496   gradually decreasing with increasing latitude (see Figure 8). Nevertheless, the high density

497   solar EUV ionized plasma will only enter the cusp region from the post-noon sector due to

498   convection [Foster, 1993]. The ionospheric plasma is mainly structured by low density plasma

499   from the pre-noon sector, i.e. 09:00 – 11:00 MLT. But sometimes the enhanced plasma can

500   initially be corotated past noon at lower latitudes, before being entrained in the afternoon

501   convection pattern and brought back toward noon [Foster, 1993; Zhang et al., 2013b]. This

502   will enhance the F-region plasma at low latitudes in the pre-noon sector [e.g., Pinnok et al.,

503   1995], while the more poleward ionospheric density and the target location of the

504   irregularities remains unchanged. The ray path will be strongly refracted by the lower latitude

505   enhanced F-region density. However, in order to allow for a propagation path to the same

506   location, a shorter ray path and smaller SWB – AEB offset will be needed [e.g. Yeoman et al.,

507   2008]. Nevertheless, the horizontal density gradient could be slightly different in the post-

508   noon sector, compared to pre-noon, because the pre-noon to post-noon ratio of

509   photoionization conductivity is ~0.33 during the winter [Hu et al., 2014]. The sharply

510 enhanced ionospheric density, resulting from the intake of high density solar EUV ionized

511 plasma, will nearly cover the whole radio wave path in the noon sector, i.e. 11:00 – 14:00

512 MLT, which will produce a strong refraction, resulting in an increased overestimation of the

513 SWB location.

514

515 **4.4. Variation with Radar Operation Frequency**

516 When the ionospheric electron density encountered with the ray is constant, a change in radar

517 frequency will result in a different refractive index for the radio wave at the same place

518 [Ponomarenko et al., 2009; Gillies et al, 2011, 2012]. In order to quantify this effect, the

519 median filtered SWB – AEB offsets as a function of the frequencies at 12:00 – 13:00 MLT

520 have been compared in Figure 6. Under nearly equal solar flux and range conditions, the

521 median filtered SWB – AEB offsets with high radar frequencies are mostly larger than with

522 relatively low radar frequencies. This implies that the varied radar frequencies modulate the

523 ray path, which could contribute to the varied SWB – AEB offset.

524

525 A multi-frequency study of radio wave refraction effects was made by André et al. [1997] at

526 solar maxima (February and September in 1988). They observed that the radio wave path (i.e.

527 SWB – AEB offset) was shifted ~20 km poleward when the radar frequency was changed

528 from 11 to 12 MHz, and ~60 km poleward for 11 to 14 MHz, which means that the refracted

529 height of the radio wave path was elevated [Milan et al., 2003a; Senior et al., 2004]. However,

530 the modeled analysis by a ray-tracing program only showed 10 km poleward shifts when the

531 radar frequency changed from 11 to 14 MHz, which was much lower than the experimental

532 data. As there is no linear trend can be easily observed in Figure 6, through averaging the

533 SWB – AEB offsets for different radar operating frequencies without taking account of the

534 range differences, the SWB – AEB offsets will, on average, shift poleward by 0.44°, 0.2° and

535 0.28° latitude for radar frequencies varied from 10 to 12.4, 12.4 to 13.2 and 11.2 to 12.4 MHz,

536 respectively. This means that the variable radar frequencies contribute to the range accuracy

537 at an order of 20, 27 and 25 km with the solar flux at 133, 202 and 84 s.f.u. for a radar

538 frequency change of 1 MHz, respectively. This is analogous to the result of André et al.

539 [1997], which suggests that the varied radar frequencies affect the refraction of the radio wave

540 differently for different F-region ionospheric densities.

541

542 **5. Conclusions**

543 A statistical comparison of the difference in latitude between the HF radar SWB and the OI

544 630.0 nm AEB, versus solar activity, MLT and radar operating frequency, have been carried

545 out in this paper. Although some mapping errors inevitably come from the assumed auroral

546 emission height, the optical mapping errors were significantly reduced by restricting the

547 location of the 630.0 nm data to be near local zenith. The inherent SWB – AEB differences

548 are therefore due to the virtual height model used by SuperDARN [Yeoman et al., 2001, 2008;

549 Chisham et al., 2008], the results show that the F-region density due to solar flux and MLT

550 variations affects the refraction of the ray path and has a critical influence on the range

551 accuracy of HF radar echoes.

552

553 A close relationship of median filtered SWB – AEB offsets with solar cycle is demonstrated.

554 The SWB – AEB offset at solar maxima is, on average, two times larger than at solar minima,

555 while some offset discrepancies with prior studies could be understood by considering the

556 different boundary finding algorithms and database used. An asymmetric distribution of SWB

557 – AEB offset versus MLT is associated with the ionospheric density at sub-auroral latitudes,

558 which is modulated by transport of high density solar EUV ionized plasma from the post-

559 noon sector, which can only be visualized using severely smoothed values from the IRI model.

560   An example of the simultaneous SWB – AEB offset and GPS TEC in Tromsø confirms this

561   speculation. Due to the intake of high density solar EUV ionized plasma from the post-noon

562   sector to the cusp region, the peaks of SWB – AEB offset versus MLT tends to be located

563   near noon. The mapped HF radar SWB will generally shift poleward in response to an

564   enhanced F-region density in the noon and post-noon sectors, while due to ray path geometry

565   the different horizontal density gradient along the geomagnetic meridian would make the

566   SWB – AEB offsets slightly different (i.e. unrelated to the ground range in the pre-noon

567   sector). The altered HF radar operating frequency also has a varied refraction effect that

568   contributes to the final location of HF radar echoes. However, the detailed relationship of the

569   SWB – AEB offset with the varied radar frequency vs. a varying ionospheric density should

570   be considered in future studies.

571

585

References:

André, R., C. Hanuise, J. P. Villain, and J. C. Cerisier (1997), HF radars: Multifrequency study of refraction effects and localization of scattering, *Radio Sci.*, *32*(1), 153-168, doi:10.1029/96rs02987.

Baker, K. B., R. A. Greenwald, A. D. M. Walker, P. F. Bythrow, L. J. Zanetti, T. A. Potemra, D. A. Hardy, F. J. Rich, and C. L. Rino (1986), A case study of plasma processes in the dayside cleft, *J. Geophys. Res.*, *91*(A3), 3130, doi:10.1029/JA091iA03p03130.

Baker, K. B., and S. Wing (1989), A new magnetic coordinate system for conjugate studies at high latitudes, *J. Geophys. Res.*, *94*(A7), 9139, doi:10.1029/JA094iA07p09139.

Baker, K. B., J. R. Dudeney, R. A. Greenwald, M. Pinnock, P. T. Newell, A. S. Rodger, N. Mattin, and C. I. Meng (1995), HF radar signatures of the cusp and low-latitude boundary layer, *J. Geophys. Res.*, *100*(A5), 7671, doi:10.1029/94ja01481.

Bilitza, D., D. Altadill, Y. Zhang, C. Mertens, V. Truhlik, P. Richards, L.-A. McKinnell, and B. Reinisch (2014), The International Reference Ionosphere 2012 - a model of international collaboration, *J. Space Weather Spac.*, *4*, A07, doi:10.1051/swsc/2014004.

Bjoland, L. M., X. Chen, Y. Jin, A. S. Reimer, Å. Skjæveland, M. R. Wessel, J. K. Burchill, L. B. N. Clausen, S. E. Haaland, and K. A. McWilliams (2015), Interplanetary magnetic field and solar cycle dependence of Northern Hemisphere *F* region joule heating, *J. Geophys. Res.*, *120*, doi:10.1002/2014JA020586.

Cai, H. T., S. Y. Ma, Y. Fan, Y. C. Liu, and K. Schlegel (2008), Climatological features of electron density in the polar ionosphere from long-term observations of EISCAT/ESR radar, *Ann. Geophys.*, *25*(12), 2561-2569, doi:10.5194/angeo-25-2561-2007.

Carlson, H. C., K. Oksavik, J. Moen, and T. Pedersen (2004), Ionospheric patch formation: Direct measurements of the origin of a polar cap patch, *Geophys. Res. Lett.*, *31*(8), doi:10.1029/2003gl018166.

Carlson, H. C., J. Moen, K. Oksavik, C. P. Nielsen, I. W. McCrea, T. R. Pedersen, and P. Gallop (2006), Direct observations of injection events of subauroral plasma into the polar cap, *Geophys. Res. Lett.*, *33*(5), doi:10.1029/2005gl025230.

Chen, X. C., D. A. Lorentzen, J. I. Moen, K. Oksavik, and L. J. Baddeley (2015), Simultaneous ground-based optical and HF radar observations of the ionospheric footprint of the open/closed field line boundary along the geomagnetic meridian, *J. Geophys. Res.*, *120*, doi:10.1002/2015JA021481.

Chisham, G., and M. P. Freeman (2003), A technique for accurately determining the cusp-region polar cap boundary using SuperDARN HF radar measurements, *Ann. Geophys.*, *21*(4), 983-996, doi:10.5194/angeo-21-983-2003.

620 Chisham, G., and M. P. Freeman (2004), An investigation of latitudinal transitions in the SuperDARN
621   Doppler spectral width parameter at different magnetic local times, *Ann. Geophys.*, *22*(4), 1187-
622   1202, doi: 10.5194/angeo-22-1187-2004.

623 Chisham, G., M. P. Freeman, M. M. Lam, G. A. Abel, T. Sotirelis, R. A. Greenwald, and M. Lester
624   (2005a), A statistical comparison of SuperDARN spectral width boundaries and DMSP particle
625   precipitation boundaries in the afternoon sector ionosphere, *Ann. Geophys.*, *23*(12), 3645-3654,
626   doi:10.5194/angeo-23-3645-2005.

627 Chisham, G., M. P. Freeman, T. Sotirelis, and R. A. Greenwald (2005b), The accuracy of using the
628   spectral width boundary measured in off-meridional SuperDARN HF radar beams as a proxy for
629   the open-closed field line boundary, *Ann. Geophys.*, *23*(7), 2599-2604, doi:10.5194/angeo-23-
630   2599-2005.

631 Chisham, G., M. P. Freeman, T. Sotirelis, R. A. Greenwald, M. Lester, and J. P. Villain (2005c), A
632   statistical comparison of SuperDARN spectral width boundaries and DMSP particle precipitation
633   boundaries in the morning sector ionosphere, *Ann. Geophys.*, *23*(3), 733-743, doi:10.5194/angeo-
634   23-733-2005.

635 Chisham, G., et al. (2007), A decade of the Super Dual Auroral Radar Network (SuperDARN):
636   scientific achievements, new techniques and future directions, *Surv. Geophys.*, *28*(1), 33-109,
637   doi:10.1007/s10712-007-9017-8.

638 Chisham, G., T. K. Yeoman, and G. J. Sofko (2008), Mapping ionospheric backscatter measured by
639   the SuperDARN HF radars - Part 1: A new empirical virtual height model, *Ann. Geophys.*, *26*(4),
640   823-841, doi:10.5194/angeo-26-823-2008.

641 Cousins, E., and S. Shepherd (2010), A dynamical model of high-latitude convection derived from
642   SuperDARN plasma drift measurements, *J. Geophys. Res.*, *115*(A12), doi: 10.1029/2010JA016017.

643 Cowley, S. (2000), Magnetosphere-ionosphere interactions: A tutorial review, *Magnetospheric*
644   *Current Systems, Geophys. Monogr. Ser.*, *118*, 91-106.

645 Danskin, D. W., A. V. Koustov, T. Ogawa, N. Nishitani, S. Nozawa, S. E. Milan, M. Lester, and D.
646   Andre (2002), On the factors controlling occurrence of F-region coherent echoes, *Ann. Geophys.*,
647   *20*(9), 1385-1397, doi:10.5194/angeo-20-1385-2002.

648 Foster, J. C. (1984), Ionospheric signatures of magnetospheric convection, *J. Geophys. Res.*, *89*(A2),
649   855-865, doi: 10.1029/JA089iA02p00855.

650 Foster, J. C. (1993), Storm time plasma transport at middle and high latitudes, *J. Geophys. Res.*,
651   *98*(A2), 1675-1689, doi:10.1029/92JA02032.

652 Foster, J. C., A. J. Coster, P. J. Erickson, F. J. Rich, and B. R. Sandel (2004), Stormtime observations
653   of the flux of plasmaspheric ions to the dayside cusp/magnetopause, *Geophys. Res. Lett.*, *31*(8),
654   doi: 10.1029/2004GL020082.

655 Foster, J. C., et al. (2005), Multiradar observations of the polar tongue of ionization, *J. Geophys. Res.*,
656   *110*(A9), doi:10.1029/2004ja010928.

657 Freeman, M. P., and G. Chisham (2004), On the probability distributions of SuperDARN Doppler
658   spectral width measurements inside and outside the cusp, *Geophys. Res. Lett.*, *31*(22),
659   doi:10.1029/2004gl020923.
660 Gillies, R. G., G. C. Hussey, G. J. Sofko, D. M. Wright, and J. A. Davies (2010), A comparison of
661   EISCAT and SuperDARNF-region measurements with consideration of the refractive index in the
662   scattering volume, *J. Geophys. Res.*, *115*(A6), doi:10.1029/2009ja014694.
663 Gillies, R. G., G. C. Hussey, G. J. Sofko, P. V. Ponomarenko, and K. A. McWilliams (2011),
664   Improvement of HF coherent radar line-of-sight velocities by estimating the refractive index in the
665   scattering volume using radar frequency shifting, *J. Geophys. Res.*, *116*(A1),
666   doi:10.1029/2010ja016043.
667 Gillies, R. G., G. C. Hussey, G. J. Sofko, and K. A. McWilliams (2012), A statistical analysis of
668   SuperDARN scattering volume electron densities and velocity corrections using a radar frequency
669   shifting technique, *J. Geophys. Res.*, *117*(A8), doi:10.1029/2012ja017866.
670 Greenwald, R. A., K. B. Baker, R. A. Hutchins, and C. Hanuise (1985), An HF phased-array radar for
671   studying small-scale structure in the high-latitude ionosphere, *Radio Sci.*, *20*(1), 63-79, doi:
672   10.1029/RS020i001p00063.
673 Greenwald, R. A., et al. (1995), DARN/SuperDARN A global view of the dynamics of high-latitude
674   convection, *Space Sci. Rev.*, *71*(1-4), 761-796, doi:10.1007/BF00751350.
675 Greenwald, R. A., K. Oksavik, R. Barnes, J. M. Ruohoniemi, J. Baker, and E. R. Talaat (2008), First
676   radar measurements of ionospheric electric fields at sub-second temporal resolution, *Geophys. Res.*
677   *Lett.*, *35*(3), doi:10.1029/2007gl032164.
678 Hu, Z.-J., Y. Ebihara, H.-G. Yang, H.-Q. Hu, B.-C. Zhang, B. Ni, R. Shi, and T. S. Trondsen (2014),
679   Hemispheric asymmetry of the structure of dayside auroral oval, *Geophys. Res. Lett.*, *41*(24),
680   8696-8703, doi:10.1002/2014gl062345.
681 Johnsen, M. G., and D. A. Lorentzen (2012a), The dayside open/closed field line boundary as seen
682   from space- and ground-based instrumentation, *J. Geophys. Res.*, *117*(A3),
683   doi:10.1029/2011ja016983.
684 Johnsen, M. G., and D. A. Lorentzen (2012b), A statistical analysis of the optical dayside open/closed
685   field line boundary, *J. Geophys. Res.*, *117*(A2), doi:10.1029/2011ja016984.
686 Johnsen, M. G., D. A. Lorentzen, J. M. Holmes, and U. P. Løvhaug (2012), A model based method for
687   obtaining the open/closed field line boundary from the cusp auroral 6300 Å[OI] red line, *J.*
688   *Geophys. Res.*, *117*(A3), doi:10.1029/2011ja016980.
689 Knudsen, W. (1974), Magnetospheric convection and the high-latitude F_2 ionosphere, *J. Geophys. Res.*,
690   *79*(7), 1046-1055, doi: 10.1029/JA079i007p01046.
691 Koustov, A., D. André, E. Turunen, T. Raito, and S. Milan (2007), Heights of SuperDARN F region
692   echoes estimated from the analysis of HF radio wave propagation, *Ann. Geophys.*, *25*(9), 1987-
693   1994, doi: 10.5194/angeo-25-1987-2007.

694 Koustov, A. V., P. V. Ponomarenko, M. Ghezelbash, D. R. Themens, and P. T. Jayachandran (2014),
695   Electron density and electric field over Resolute Bay and F region ionospheric echo detection with
696   the Rankin Inlet and Inuvik SuperDARN radars, *Radio Sci.*, *49*(12), 1194-1205,
697   doi:10.1002/2014RS005579.

698 Lester, M., P. J. Chapman, S. W. H. Cowley, S. J. Crooks, J. A. Davies, P. Hamadyk, K. A.
699   McWilliams, S. E. Milan, M. J. Parsons, and D. B. Payne (2004), Stereo CUTLASS-A new
700   capability for the SuperDARN HF radars, *Ann. Geophys.*, *22*(2), 459-473, doi:10.5194/angeo-22-
701   459-2004.

702 Liou, K., P. T. Newell, C. I. Meng, M. Brittnacher, and G. Parks (1998), Characteristics of the solar
703   wind controlled auroral emissions, *J. Geophys. Res.*, *103*(A8), 17543, doi:10.1029/98ja01388.

704 Liu, E. X., H. Q. Hu, R. Y. Liu, Z. S. Wu, and M. Lester (2012), An adjusted location model for
705   SuperDARN backscatter echoes, *Ann. Geophys.*, *30*(12), 1769-1779, doi:10.5194/angeo-30-1769-
706   2012.

707 Lockwood, M., P. E. Sandholt, S. W. H. Cowley, and T. Oguti (1989), Interplanetary magnetic field
708   control of dayside auroral activity and the transfer of momentum across the dayside magnetopause,
709   *Planet. Space Sci.*, *37*(11), doi:10.1016/0032-0633(89)90106-2.

710 Lockwood, M., S. W. H. Cowley, and M. P. Freeman (1990), The excitation of plasma convection in
711   the high-latitude ionosphere, *J. Geophys. Res.*, *95*(A6), 7961, doi:10.1029/JA095iA06p07961.

712 Lockwood, M., and H. C. Carlson (1992), Production of polar cap electron density patches by
713   transient magnetopause reconnection, *Geophys. Res. Lett.*, *19*(17), 1731-1734,
714   doi:10.1029/92GL01993.

715 Lointier, G., T. Dudok de Wit, C. Hanuise, X. Vallières, and J.-P. Villain (2008), A statistical
716   approach for identifying the ionospheric footprint of magnetospheric boundaries from
717   SuperDARN observations, *Ann. Geophys.*, *26*(2), 305-314, doi:10.5194/angeo-26-305-2008.

718 Lorentzen, D. A., C. S. Deehr, J. I. Minow, R. W. Smith, H. C. Stenbaek-Neielsen, F. Sigernes, R. L.
719   Arnoldy, and K. Lynch (1996), SCIFER-Dayside auroral signatures of magnetospheric energetic
720   electrons, *Geophys. Res. Lett.*, *23*(14), 1885-1888, doi:10.1029/96gl00593.

721 Lorentzen, D. A., J. Moen, K. Oksavik, F. Sigernes, Y. Saito, and M. G. Johnsen (2010), In situ
722   measurement of a newly created polar cap patch, *J. Geophys. Res.*, *115*(A12),
723   doi:10.1029/2010ja015710.

724 Milan, S. E., T. K. Yeoman, M. Lester, E. C. Thomas, and T. B. Jones (1997), Initial backscatter
725   occurrence statistics from the CUTLASS HF radars, *Ann. Geophys.*, *15*(6), 703-718,
726   doi:10.1007/s00585-997-0703-0.

727 Milan, S. E., T. K. Yeoman, and M. Lester (1998), The dayside auroral zone as a hard target for
728   coherent HF radars, *Geophys. Res. Lett.*, *25*(19), 3717-3720, doi:10.1029/98gl02781.

729   Milan, S. E., M. Lester, S. W. H. Cowley, J. Moen, P. E. Sandholt, and C. J. Owen (1999), Meridian-
730   scanning photometer, coherent HF radar, and magnetometer observations of the cusp: a case study,
731   *Ann. Geophys.*, *17*(2), 159-172, doi:10.1007/s00585-999-0159-5.

732   Milan, S., M. Lester, and N. Sato (2003a), Multi-frequency observations of E-region HF radar aurora,
733   *Ann. Geophys.*, *21*(3), 761-777.

734   Milan, S. E., M. Lester, S. Cowley, K. Oksavik, M. Brittnacher, R. Greenwald, G. Sofko, and J.-P.
735   Villain (2003b), Variations in the polar cap area during two substorm cycles, *Ann. Geophys.*, *21*(5),
736   1121-1140, doi:10.5194/angeo-21-1121-2003.

737   Milan, S. E., J. S. Gosling, and B. Hubert (2012), Relationship between interplanetary parameters and
738   the magnetopause reconnection rate quantified from observations of the expanding polar cap, *J.
739   Geophys. Res.*, *117*(A3), doi:10.1029/2011ja017082.

740   Moen, J., M. Lockwood, P. Sandholt, U. Løvhaug, W. Denig, A. Van Eyken, and A. Egeland (1996),
741   Variability of dayside high latitude convection associated with a sequence of auroral transients, *J.
742   Atmos. Terr. Phys.*, *58*(1), 85-96, doi:10.1016/0021-9169(95)00021-6.

743   Moen, J., D. A. Lorentzen, and F. Sigernes (1998), Dayside moving auroral forms and bursty proton
744   auroral events in relation to particle boundaries observed by NOAA 12, *J. Geophys. Res.*, *103*(A7),
745   14855, doi:10.1029/97ja02877.

746   Moen, J., H. C. Carlson, S. E. Milan, N. Shumilov, B. Lybekk, P. E. Sandholt, and M. Lester (2001),
747   On the collocation between dayside auroral activity and coherent HF radar backscatter, *Ann.
748   Geophys.*, *18*(12), 1531-1549, doi:10.1007/s00585-001-1531-2.

749   Moen, J., I. K. Walker, L. Kersley, and S. E. Milan (2002), On the generation of cusp HF backscatter
750   irregularities, *J. Geophys. Res.*, *107*(A4), doi:10.1029/2001ja000111.

751   Moen, J., M. Lockwood, K. Oksavik, H. Carlson, W. Denig, A. Van Eyken, and I. McCrea (2004),
752   The dynamics and relationships of precipitation, temperature and convection boundaries in the
753   dayside auroral ionosphere, *Ann. Geophys.*, *22*(6), 1973-1987, doi:10.5194/angeo-22-1973-2004.

754   Moen, J., H. C. Carlson, K. Oksavik, C. P. Nielsen, S. E. Pryse, H. R. Middleton, I. W. McCrea, and P.
755   Gallop (2006), EISCAT observations of plasma patches at sub-auroral cusp latitudes, *Ann.
756   Geophys.*, *24*(9), 2363-2374, doi:10.5194/angeo-24-2363-2006.

757   Moen, J., X. C. Qiu, H. C. Carlson, R. Fujii, and I. W. McCrea (2008), On the diurnal variability in
758   F2-region plasma density above the EISCAT Svalbard radar, *Ann. Geophys.*, *26*(8), 2427-2433,
759   doi:10.5194/angeo-26-2427-2008.

760   Moen, J., K. Oksavik, T. Abe, M. Lester, Y. Saito, T. A. Bekkeng, and K. S. Jacobsen (2012), First in-
761   situ measurements of HF radar echoing targets, *Geophys. Res. Lett.*, *39*(7), L07104,
762   doi:10.1029/2012gl051407.

763   Moen, J., K. Oksavik, L. Alfonsi, Y. Daabakk, V. Romano, and L. Spogli (2013), Space weather
764   challenges of the polar cap ionosphere, *J. Space Weather Spac.*, *3*, A02,
765   doi:10.1051/swsc/2013025.

Newell, P. T., and C. I. Meng (1992), Mapping the dayside ionosphere to the magnetosphere according to particle precipitation characteristics, *Geophys. Res. Lett.*, *19*(6), 609-612, doi:0094-8534/92/92GL-00404.

Nishimura, Y., et al. (2014), Day-night coupling by a localized flow channel visualized by polar cap patch propagation, *Geophysical Research Letters*, *41*(11), 3701-3709, doi:10.1002/2014gl060301.

Oksavik, K., F. Søraas, J. Moen, and W. J. Burke (2000), Optical and particle signatures of magnetospheric boundary layers near magnetic noon: Satellite and ground-based observations, *J. Geophys. Res.*, *105*(A12), 27555, doi:10.1029/1999ja000237.

Oksavik, K., J. Moen, and H. C. Carlson (2004a), High-resolution observations of the small-scale flow pattern associated with a poleward moving auroral form in the cusp, *Geophys. Res. Lett.*, *31*(11), doi:10.1029/2004gl019838.

Oksavik, K., F. Søraas, J. Moen, R. Pfaff, J. A. Davies, and M. Lester (2004b), Simultaneous optical, CUTLASS HF radar, and FAST spacecraft observations: signatures of boundary layer processes in the cusp, *Ann. Geophys.*, *22*(2), 511-525, doi:10.5194/angeo-22-511-2004.

Oksavik, K., J. M. Ruohoniemi, R. A. Greenwald, J. B. H. Baker, J. Moen, H. C. Carlson, T. K. Yeoman, and M. Lester (2006), Observations of isolated polar cap patches by the European Incoherent Scatter (EISCAT) Svalbard and Super Dual Auroral Radar Network (SuperDARN) Finland radars, *J. Geophys. Res.*, *111*(A5), doi:10.1029/2005ja011400.

Oksavik, K., V. L. Barth, J. Moen, and M. Lester (2010), On the entry and transit of high-density plasma across the polar cap, *J. Geophys. Res.*, *115*(A12), doi:10.1029/2010ja015817.

Oksavik, K., J. I. Moen, E. H. Rekaa, H. C. Carlson, and M. Lester (2011), Reversed flow events in the cusp ionosphere detected by SuperDARN HF radars, *J. Geophys. Res.*, *116*(A12), doi:10.1029/2011ja016788.

Oksavik, K., J. Moen, M. Lester, T. A. Bekkeng, and J. K. Bekkeng (2012), In situ measurements of plasma irregularity growth in the cusp ionosphere, *J. Geophys. Res.*, *117*(A11), doi:10.1029/2012ja017835.

Pinnock, M., A. Rodger, and F. Berkey (1995), High-latitude F region electron concentration measurements near noon: A case study, *J. Geophys. Res.*, *100*(A5), 7723-7729, doi: 10.1029/94JA02558.

Ponomarenko, P. V., and C. L. Waters (2006), Spectral width of SuperDARN echoes: measurement, use and physical interpretation, *Ann. Geophys.*, *24*(1), 115-128, doi:10.5194/angeo-24-115-2006.

Ponomarenko, P. V., C. L. Waters, and F. W. Menk (2007), Factors determining spectral width of HF echoes from high latitudes, *Ann. Geophys.*, *25*, 675–687, doi:10.5194/angeo-25-675-2007.

Ponomarenko, P. V., J.-P. St-Maurice, C. L. Waters, R. G. Gillies, and A. V. Koustov (2009), Refractive index effects on the scatter volume location and Doppler velocity estimates of ionospheric HF backscatter echoes, *Ann. Geophys.*, *27*(11), 4207-4219, doi:10.5194/angeo-27-4207-2009.

803   Ponomarenko, P. V., A. V. Koustov, J. P. St.-Maurice, and J. Wiid (2011), Monitoring the F-region
804   peak electron density using HF backscatter interferometry, *Geophys. Res. Lett.*, *38*(21), L21102,
805   doi:10.1029/2011gl049675.

806   Rideout, W., and A. Coster (2006), Automated GPS processing for global total electron content data,
807   *GPS Solut.*, *10*(3), 219-228, doi: 10.1007/s10291-006-0029-5.

808   Rodger, A. S., S. B. Mende, T. J. Rosenberg, and K. B. Baker (1995), Simultaneous optical and HF
809   radar observations of the ionospheric cusp, *Geophys. Res. Lett.*, *22*(15), 2045-2048,
810   doi:10.1029/95GL01797.

811   Romick, G. J. (1976), The detection and study of the visible spectrum of the aurora and airglow, in
812   *Proc. SPIE, Methods Atmos. Radiometry*, vol. 0091, pp. 63–70, Alaska, Univ., Fairbanks, Alaska,
813   doi:10.1117/12.955072.

814   Ruohoniemi, J. M., and R. A. Greenwald (1997), Rates of scattering occurrence in routine HF radar
815   observations during solar cycle maximum, *Radio Sci.*, *32*(3), 1051-1070, doi:10.1029/97rs00116.

816   Sandholt, P. E., C. J. Farrugia, J. Moen, Ø. Noraberg, B. Lybekk, T. Sten, and T. Hansen (1998), A
817   classification of dayside auroral forms and activities as a function of interplanetary magnetic field
818   orientation, *J. Geophys. Res.*, *103*(A10), 23325, doi:10.1029/98ja02156.

819   Senior, A., N. Borisov, M. Kosch, T. Yeoman, F. Honary, and M. Rietveld (2004), Multi-frequency
820   HF radar measurements of artificial F-region field-aligned irregularities, *Ann. Geophys.*, *22*, 3503-
821   3512, doi:10.5194/angeo-22-3503-2004.

822   Sojka, J. J., M. Bowline, and R. W. Schunk (1994), Patches in the polar ionosphere: UT and seasonal
823   dependence, *J. Geophys. Res.*, *99*(A8), 14959-14970, doi:10.1029/93JA03327.

824   Sotirelis, T., J. M. Ruohoniemi, R. J. Barnes, P. T. Newell, R. A. Greenwald, J. P. Skura, and C. I.
825   Meng (2005), Comparison of SuperDARN radar boundaries with DMSP particle precipitation
826   boundaries, *J. Geophys. Res.*, *110*(A6), doi:10.1029/2004ja010732.

827   Tobiska, W. K., T. Woods, F. Eparvier, R. Viereck, L. Floyd, D. Bouwer, G. Rottman, and O. White
828   (2000), The SOLAR2000 empirical solar irradiance model and forecast tool, *J. Atmos. Sol.-Terr.*
829   *Phy.*, *62*(14), 1233-1250, doi:10.1016/S1364-6826(00)00070-5.

830   Vallières, X., J. P. Villain, and R. André (2003), Characterization of frequency effect in SuperDARN
831   spectral width distributions, *Radio Sci.*, *38*(1), 3-1-3-12, doi:10.1029/2001rs002550.

832   Villain, J. P., R. A. Greenwald, and J. F. Vickrey (1984), HF ray tracing at high latitudes using
833   measured   meridional   electron   density   distributions,   *Radio   Sci.*,   *19*(1),   359-374,
834   doi:10.1029/RS019i001p00359.

835   Woods, T. N., F. G. Eparvier, S. M. Bailey, P. C. Chamberlin, J. Lean, G. J. Rottman, S. C. Solomon,
836   W. K. Tobiska, and D. L. Woodraska (2005), Solar EUV Experiment (SEE): Mission overview
837   and first results, *J. Geophys. Res.*, *110*(A1), *A01312, doi:10.1029/2004JA010765.*

838   Yeoman, T. K., D. M. Wright, A. J. Stocker, and T. B. Jones (2001), An evaluation of range accuracy

839   in the Super Dual Auroral Radar Network over-the-horizon HF radar systems, *Radio Sci.*, *36*(4),

840   801-813, doi:10.1029/2000rs002558.

841   Yeoman, T. K., G. Chisham, L. J. Baddeley, R. S. Dhillon, T. J. T. Karhunen, T. R. Robinson, A.

842   Senior, and D. M. Wright (2008), Mapping ionospheric backscatter measured by the SuperDARN

843   HF radars - Part 2: Assessing SuperDARN virtual height models, *Ann. Geophys.*, *26*(4), 843-852,

844   doi:10.5194/angeo-26-843-2008.

845   Zhang, Q. H., et al. (2011), On the importance of interplanetary magnetic field |By| on polar cap patch

846   formation, *J. Geophys. Res.*, *116*(A5), A05308, doi:10.1029/2010ja016287.

847   Zhang, Q. H., et al. (2013a), Direct observations of the evolution of polar cap ionization patches,

848   *Science*, *339*(6127), 1597-1600, doi:10.1126/science.1231487.

849   Zhang, Q. H., B. C. Zhang, J. Moen, M. Lockwood, I. W. McCrea, H. G. Yang, H. Q. Hu, R. Y. Liu, S.

850   R. Zhang, and M. Lester (2013b), Polar cap patch segmentation of the tongue of ionization in the

851   morning convection cell, *Geophys. Res. Lett.*, *40*(12), 2918-2922, doi: 10.1002/grl.50616.

852   Zhang, Q. H., M. Lockwood, J. Foster, S. R. Zhang, B. C. Zhang, I. McCrea, J. Moen, M. Lester, and J.

853   M. Ruohoniemi (2015), Direct observations of the full Dungey convection cycle in the polar

854   ionosphere for southward interplanetary magnetic field conditions, *J. Geophys. Res.*, *120,* 4519-

855   4530*, doi: 10.1002/2015JA021172.*

856

857 **Figure Captions:**

858 **Figure 1.** Field-of-view of the SuperDARN Finland radar (grey shading) and the MSP

859 meridian (red line) in AACGM coordinates at 09:30 UT. Radar beams 5 and 9 intersect

860 Tromsø and Longyearbyen, respectively. The statistical location of the auroral oval is also

861 indicated for $K_p = 1$.

862

863 **Figure 2.** An example of the simultaneous (a) MSP Keogram for the OI 630.0 nm auroral

864 emission and (b) median filtered ionospheric spectral width observations from the

865 SuperDARN Finland radar. The vertical axes are AACGM latitude, and time runs along the

866 horizontal axis. The black dashed curve in each panel represents the identified AEB and SWB,

867 respectively.

868

869 **Figure 3.** (a) The number of days (grey bars) and individual data points (red item) for each

870 winter season. The latitudinal normalized occurrences of (b) AEB and (c) SWB from the MSP

871 and HF radar observations, respectively. (d) The variation (with standard deviation represents

872 error bars) of SWB – AEB offset in latitude along the magnetic meridian. (e) The monthly

873 averaged $F_{10.7}$ solar flux. (f) The distribution of data points by different HF radar operating

874 frequencies.

875

876 **Figure 4.** The distribution of data points versus MLT for different radar frequencies at solar

877 (a) maxima and (b) minima. (c) The distribution of the AEB (red) and the SWB (grey) versus

878 MLT for the radar frequency of 12.4 MHz. (d) The AEB versus MLT for radar frequencies of

879 10.0 MHz (black), 11.2 MHz (green) and 12.4 MHz (red) at solar minima. The corresponding

880 SWB – AEB offset versus MLT at solar (e) maxima and (f) minima.

881

882   **Figure 5.** Scatter plots of SWB – AEB offset versus AEB latitude at solar maxima (red) and

883   minima (black). The dots show observations before 11:00 MLT, while the stars represent

884   observations after that.

885

886   **Figure 6**. The distributions of median filtered SWB – AEB offsets with latitude for different

887   radar operating frequencies at three different solar fluxes (a, b, c). The bar plots represent the

888   distribution of data points, while colors illustrate the different radar operating frequencies.

889

890   **Figure 7.** An example of simultaneous SWB – AEB offsets and ionospheric TEC from a GPS

891   receiver at Tromsø. (a) The IMF B_y and B_z components from the ACE satellite. (b) The

892   observed SWB – AEB offset versus time indicated by black dots. The error bars represent the

893   probable mapping error from the assumed auroral emission height. The IMF clock angle is

894   overlaid as a magenta curve. (c) The vertical TEC from Tromsø.

895

896   **Figure 8.** An illustration of the averaged NmF_2 distributions derived from the IRI-2012 model

897   in December/January. The resolution of the color coded grid cells is one hour MLT and two

898   degrees geomagnetic latitude. Overlaid are the average convection pattern and the field-of-

899   view of the SuperDARN Finland radar. See text for more details.
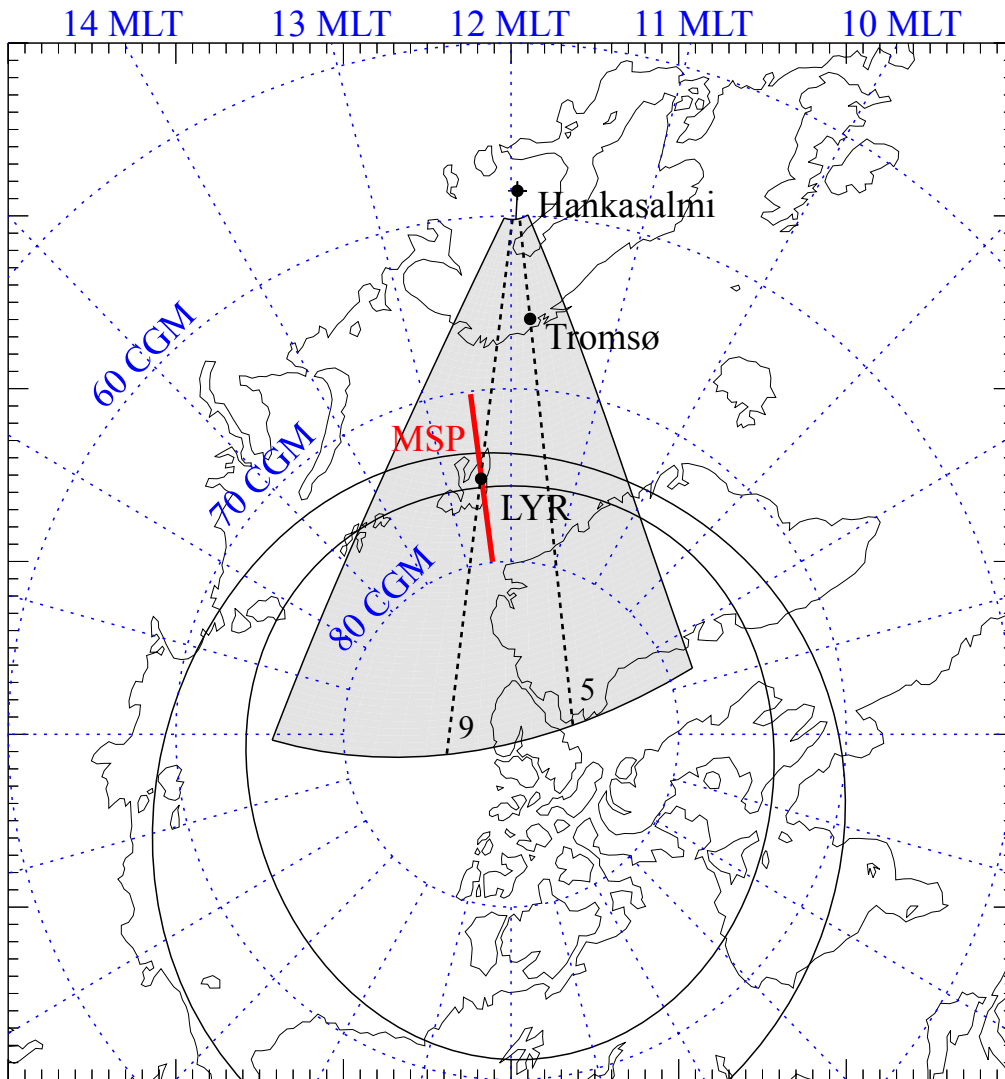
Longyearbyen MSP 31 Dec. 2003 (630.0 nm)
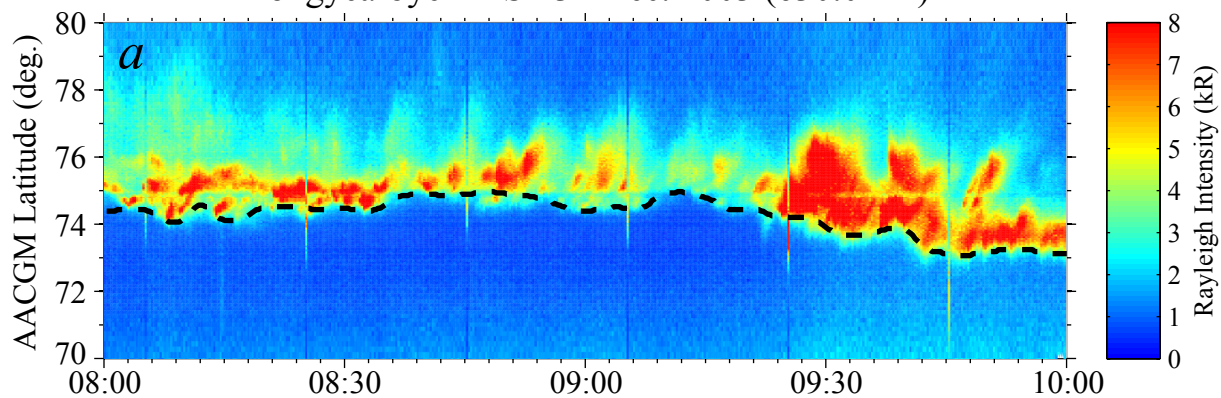
SuperDARN Hankasalmi Plot 20031231

Universal Time
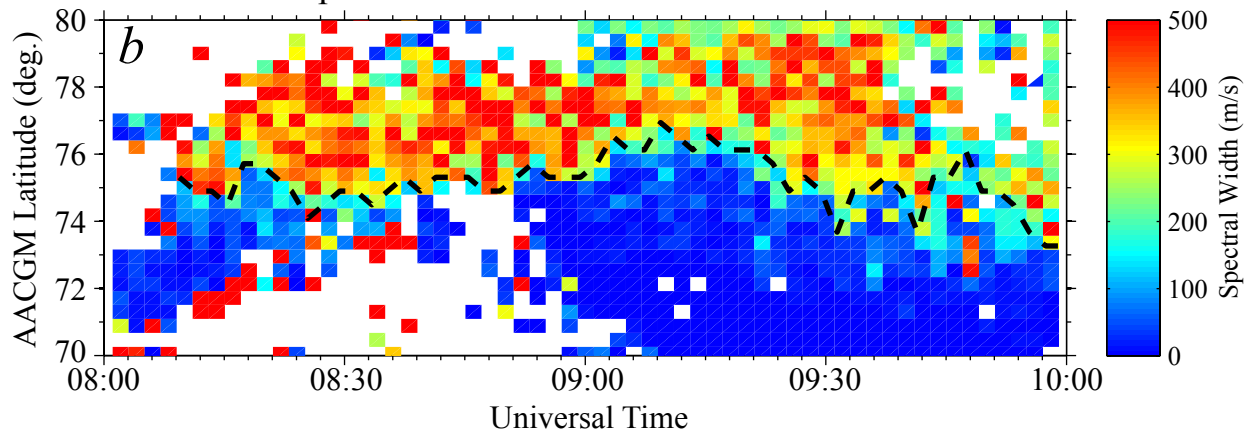
Winter season (from December to January)
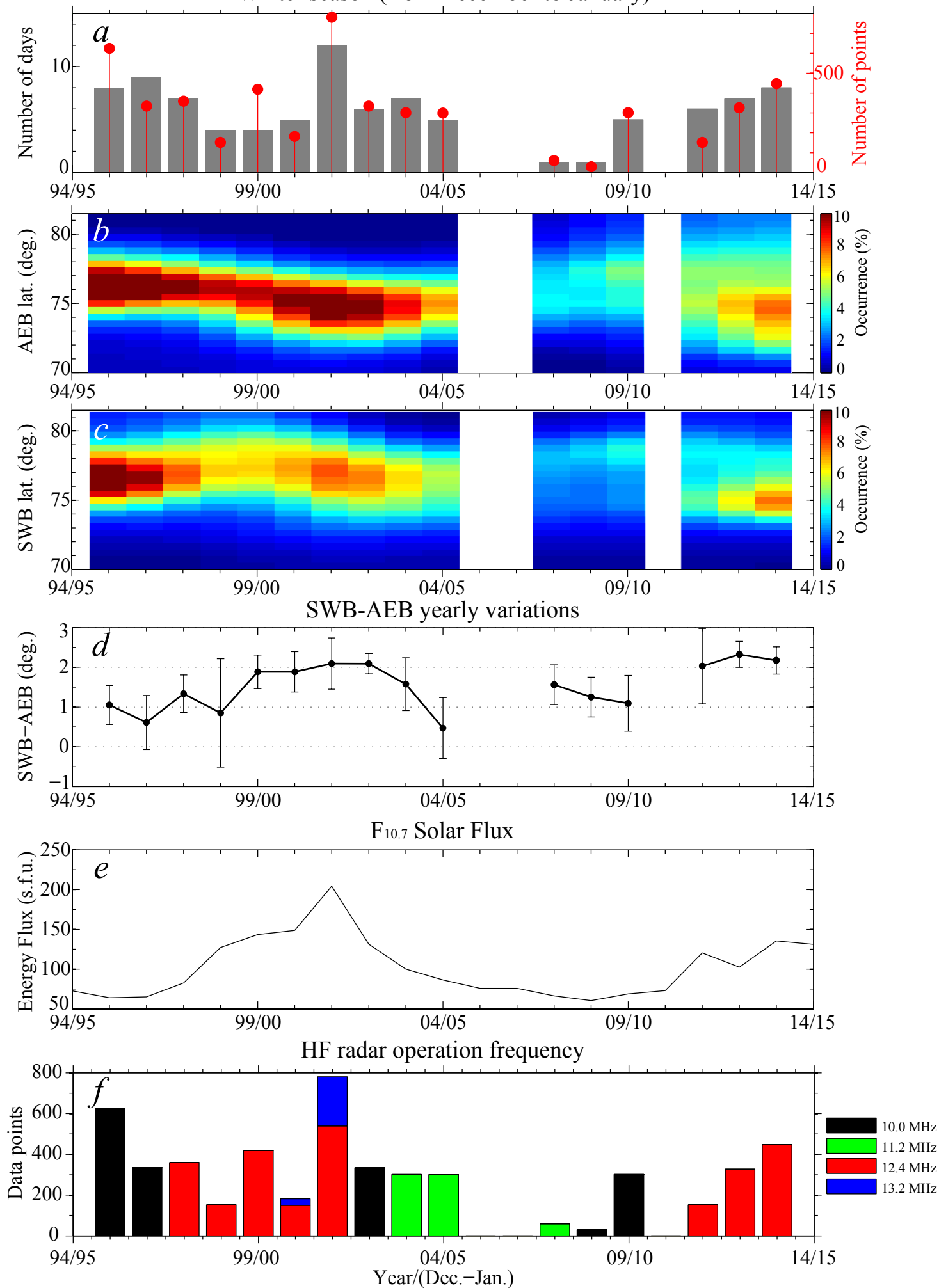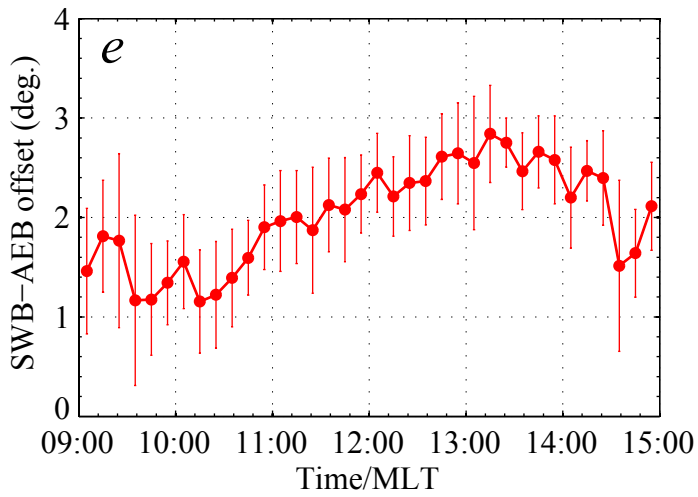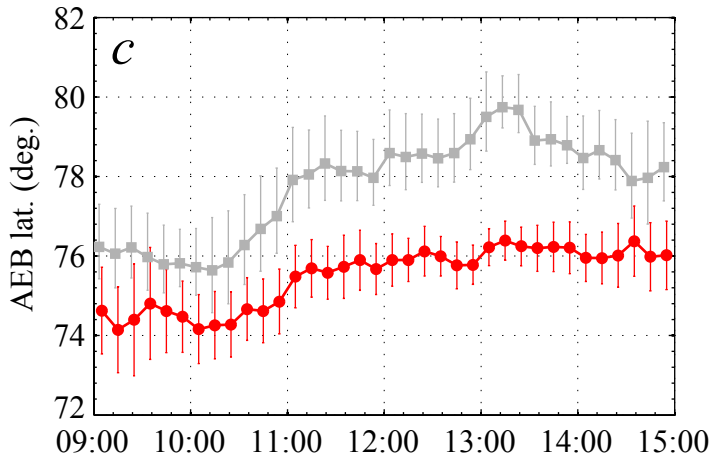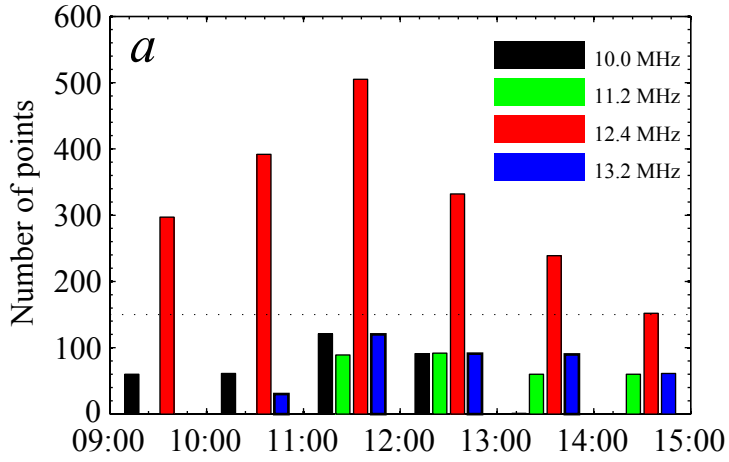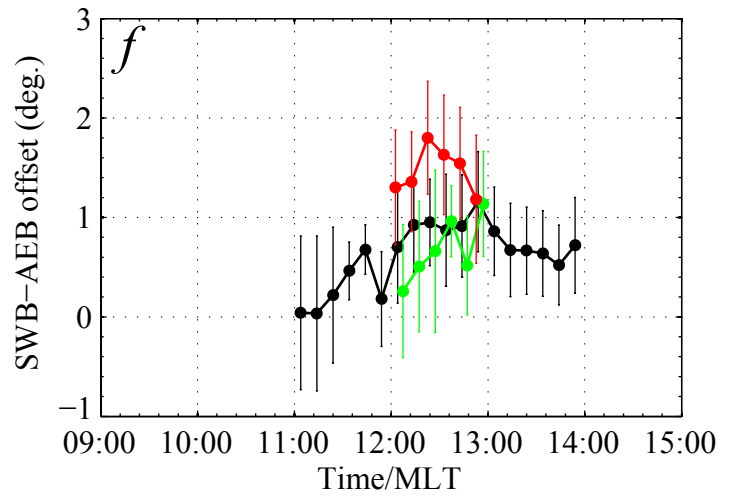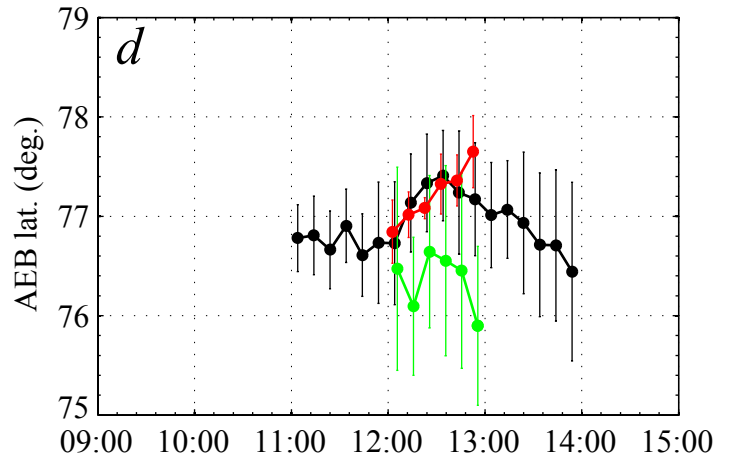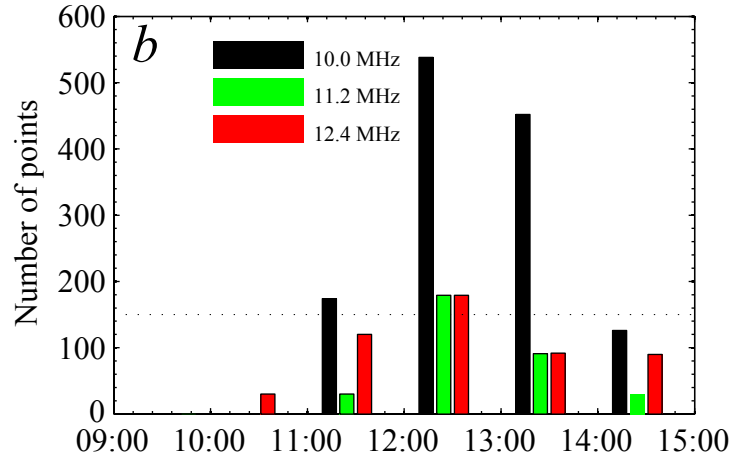
Solar Maxima at 12.4 MHz & Minima at 10 MHz

● 09:00 - 11:00 MLT
✳ 11:00 - 14:00 MLT

AEB = 0.48 × offset + 76.6º
r = 0.58

AEB = 0.72 × offset + 74.2º
r = 0.77

AEB = − 0.03 × offset + 74.5º

AEB lat. (deg.)

SWB−AEB offset (deg.)

Solar Flux at ~133 s.f.u.

Solar Flux at ~202 s.f.u.

Solar Flux at ~84 s.f.u.

ACE IMF Data

a Time lag: 61 min — By — Bz

IMFB$_{SW}$ nT

SWB-AEB offsets

b

SWB-AEB lat. (deg.)

Clock Angle (deg.)

Zenith TEC from Tromsø site

c Tromsø, Lat = 69.6°

TEC units

Universal Time (31 Dec. 2003)
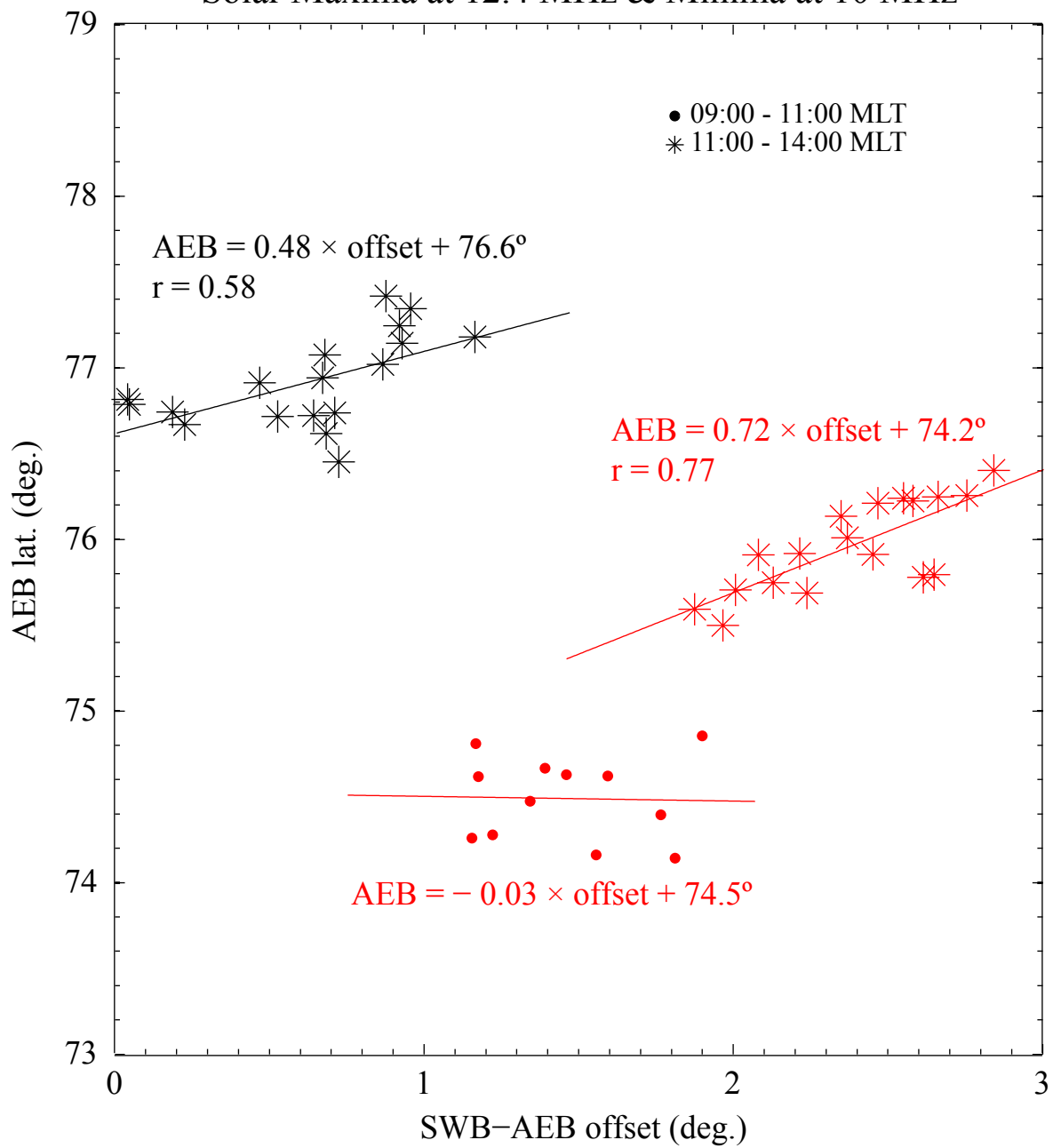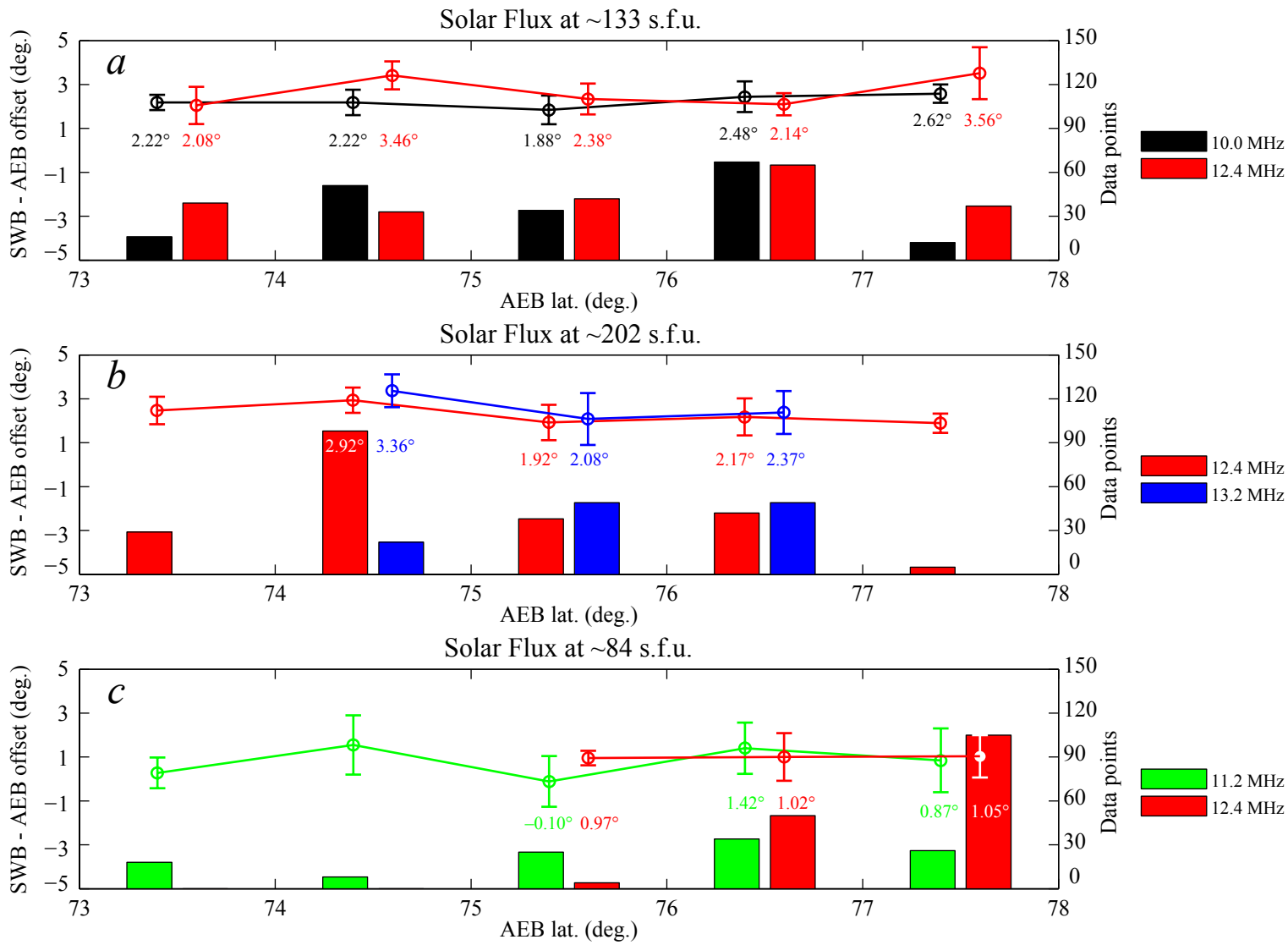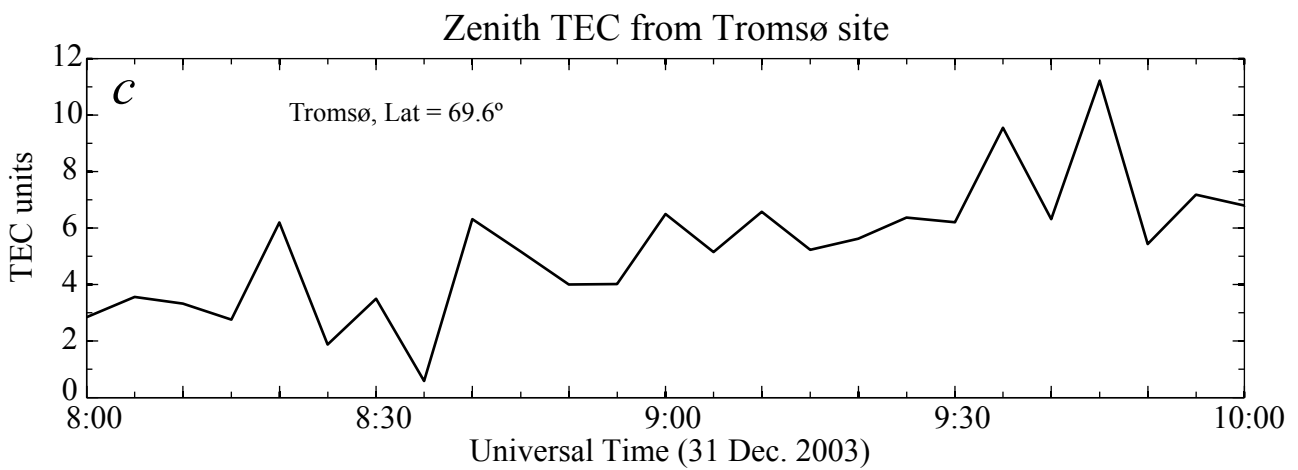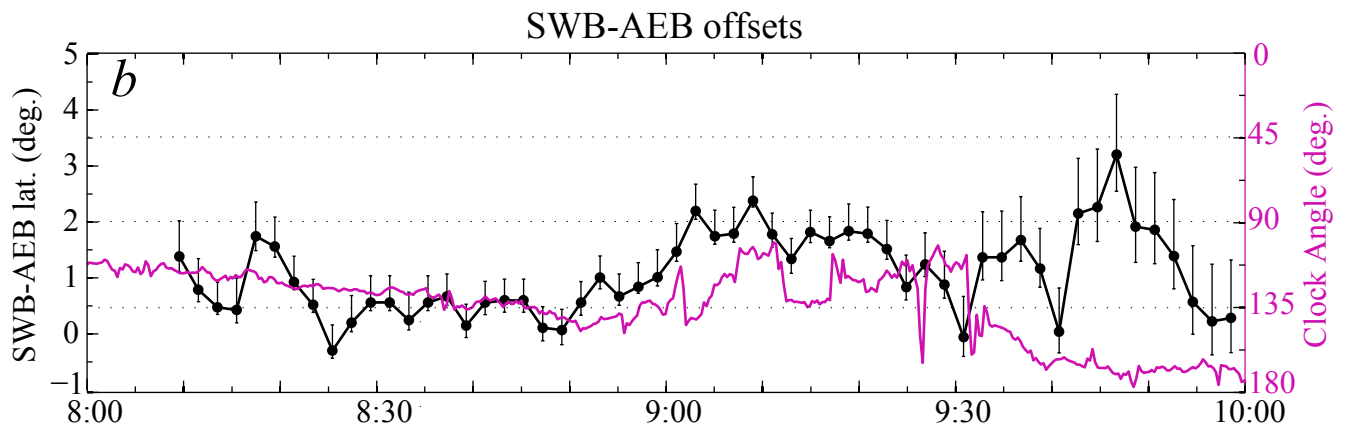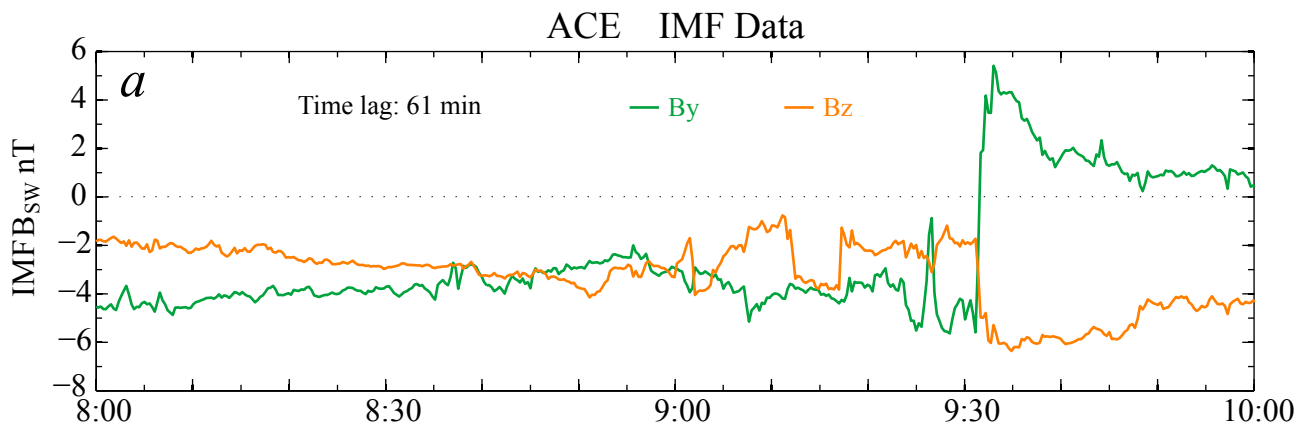
Averaged NmF2 from IRI-2012 model

CUTLASS
Finland Radar

12 MLT

18 MLT

06 MLT

70 MLAT   80 MLAT   80 MLAT   70 MLAT

$\times 10^{11}$

1   2   3   4   5

Electron density (m^{-3})